G. Sinibaldi, A. Occhicone, F. Alves Pereira, D. Caprini, L. Marino, F. Michelotti, and C. M. Casciola

View Online **Export Citation** **CrossMark**

ARTICLES YOU MAY BE INTERESTED IN

Physics of Fluids

Laser induced cavitation: Plasma generation and breakdown shockwave

View Online   Export Citation   CrossMark

G. Sinibaldi,[1,a]   A. Occhicone,[2]   F. Alves Pereira,[3]   D. Caprini,[4]   L. Marino,[1]   F. Michelotti,[2] and C. M. Casciola[1]

AFFILIATIONS

[1] Dipartimento di Ingegneria Meccanica e Aerospaziale, Sapienza Università di Roma, Via Eudossiana 18, 00184 Roma, Italy
[2] Dipartimento di Scienze di Base e Applicate per l'Ingegneria, Sapienza Università di Roma, Via A. Scarpa 14, 00161 Roma, Italy
[3] CNR-INM, Via di Vallerano 139, 00128 Roma, Italy
[4] CLNS, Istituto Italiano di Tecnologia, Viale Regina Elena 291, 00161 Roma, Italy

[a] Electronic mail: giorgia.sinibaldi@uniroma1.it

ABSTRACT

Laser induced cavitation is one of the effective techniques to generate controlled cavitation bubbles, both for basic study and for applications in different fields of engineering and medicine. Unfortunately, control of bubble formation and symmetry is hardly achieved due to a series of concurrent causes. In particular, the need to focus the laser beam at the bubble formation spot leads, in general, to a conical region proximal to the light source where conditions are met for plasma breakdown. A finite sized region then exists where the electric field may fluctuate depending on several disturbing agents, leading to possible plasma fragmentation and plasma intensity variation. Such irregularities may induce asymmetry in the successive bubble dynamics, a mostly undesired effect if reproducible conditions are sought for. In the present paper, the structure of the breakdown plasma and the ensuing bubble dynamics are analyzed by means of high speed imaging and intensity measurements of the shockwave system launched at breakdown. It is found that the parameters of the system can be tuned to optimize repeatability and sphericity. In particular, symmetric rebound dynamics is achieved almost deterministically when a pointlike plasma is generated at the breakdown threshold energy. Spherical symmetry is also favored by a large focusing angle combined with a relatively large pulse energy, a process which, however, retains a significant level of stochasticity. Outside these special conditions, the elongated and often fragmented conical plasma shape is found to be correlated with anisotropic and multiple breakdown shockwave emission.

I. INTRODUCTION

Cavitation in liquids is an intriguing phenomenon with substantial impact in engineering, medicine, and fundamental physics spanning a wide range of time scales.[25] Cavitation bubbles are traditionally associated with erosion damage,[29] e.g., in ship propellers and hydraulic turbomachinery,[27] biomedical applications,[5] e.g., cell poration[16,33] and drug delivery,[28] and microfluidics.[51] The formation of vapor nuclei may be caused by energy fluctuations of the system (homogeneous nucleation).[8] In the present work, the energy needed to form the bubble is provided by a pulsed laser light focused in and absorbed by the water medium, a process known as laser induced cavitation where the bubble formation is mediated by the breakdown of water through the generation of a plasma. In medicine, laser induced breakdown plasmas have been used to ablate fatty depositions from blood vessel walls (laser angioplasty), for fragmentation of kidney stones (lithotripsy)[50] and in ophthalmic microsurgery.[11,52] Laser based techniques for the generation of bubbles have been widely explored in the last few decades (see, e.g., Refs. 1, 6, 7, 9, 12–15, 17, 22, 24, 35, 38, 40, 41, 43–45, and 47–49). This is a stochastic process whose probability increases with the laser electric field.[32] Given the optical setup, a threshold energy is needed before the plasma forms. Here, the threshold energy is defined as the energy at which plasma is observed with 50% probability.[43,45]

Once the breakdown threshold is reached, enough energy is absorbed in the focus region so that a small liquid volume heats up to ionization temperatures (several thousand kelvin) generating a plasma and subsequently releasing a shockwave. As the shockwave propagates in the liquid, a vapor bubble is left in the focus region, which is not in equilibrium with the surrounding liquid. According to the accepted Rayleigh-Plesset (RP) model,[30] the evolution of a spherical bubble of radius r is described by the following equation:

$$\frac{p_V - p_e}{\rho_L} = r\ddot{r} + \frac{3}{2}\dot{r}^2 + \frac{4\nu_L}{r}\dot{r} + \frac{2\sigma}{\rho_L r}, \tag{1}$$

where p_e is the ambient pressure, p_V is the vapor pressure (2.33 kPa in water at 20 °C), $\sigma = 7.73 \times 10^{-2}$ Pa m is the liquid/vapor surface tension, ρ_L is the liquid density, and ν_L is the liquid kinematic viscosity. For water at room temperature and ambient pressure, $p_e = 0.1$ MPa, the surface tension is entirely negligible for millimeter bubbles. Typically, the effect of viscosity, appearing in Eq. (1) through the boundary conditions at the bubble interface,[4] is also negligible. In these conditions, the energy deposited by the laser beam is partially radiated away by the breakdown shockwave and in part provides the conserved energy E_0 associated with the bubble dynamics. The energy balance reads $E_K + E_B = E_0$, where E_K basically is the kinetic energy of the liquid (the kinetic energy share of the vapor being practically irrelevant) and $E_B = 4/3\pi(p_e - p_V)r^3$ is the bubble potential energy. The bubble expands until all the energy is converted into bubble potential energy, providing an equation relating the bubble energy to the maximum radius r_{max},

$$E_0 = E_B = \frac{4}{3}\pi(p_e - p_V)r_{max}^3. \tag{2}$$

Once the maximum radius is reached, the bubble starts compressing back until the eventual collapse (at maximum radius, $\dot{r}$ vanishes, and $\ddot{r} < 0$, as follows from the RP equation). At the final stage of the collapse, luminescence in the form of a light flash can be observed[25] and a second shockwave is launched into the liquid. A second bubble forms out of a rebound process, and the newly formed bubble expands. Ideally, the process is repeated until the energy is dissipated by viscosity, dispersed by thermal conduction from the hotter compressed bubble to the colder surrounding liquid, or radiated by shockwaves.[18,19] In fact, the dynamics is not exactly spherically symmetric for several reasons to be further discussed below. The time interval between the bubble maximum expansion and the end of the collapse phase is the Rayleigh collapse time[31] $T_c = 0.915 r_{max}\sqrt{\rho_L/(p_e - p_V)}$.

The present experimental study is focused on laser induced cavitation bubbles in pure water addressing, in particular, the repeatability of the process and the sphericity of the ensuing bubble dynamics. These features are affected by many factors such as laser stability, e.g., in terms of pulse energy, the specific optical setup, and the possible presence of impurities dispersed in water. A key aspect is the shape of the plasma formed at breakdown, here studied by visualization and through pressure measurements aimed at characterizing the breakdown shockwave using a custom made fiber optic probe hydrophone (FOPH). The effect of the plasma shape is evaluated by investigating the bubble dynamics up to the first rebound (namely, up to the formation and collapse of the second bubble) through high speed imaging. The main purpose is to optimize the conditions for achieving a repeatable spherically symmetric plasma-bubble-rebound configuration.

II. EXPERIMENTAL SETUP

With reference to Fig. 1, the experimental setup can be schematically divided into three main parts:[23,35] an apparatus for bubble nucleation (a), a video acquisition system (b), and a hydrophone system (c).

A. Laser induced cavitation setup

Bubbles are induced by focusing a pulsed laser in a cavitation box filled with pure water (Milli-Q water, 0.22 μm membrane filter) and equipped with a parabolic mirror,[22] used to focus the beam. The laser is a frequency-doubled Q-switched Nd:YAG (Litron Nano S 35-15), which can deliver light pulses at the wavelength $\lambda = 532$ nm, with duration $\tau = 8$ ns at a repetition rate that can be tuned in the range of 0–15 Hz and pulse energy up to 30 mJ. It is known that ns-pulses create a higher electron density than picosecond-pulses, resulting in higher absorption coefficient of the plasma, stronger plasma radiation, higher plasma temperature, and stronger mechanical effects.[46] The energy at the laser exit, E_L, is sampled by an energy sensor through a beam splitter (4%) (see Fig. 1).
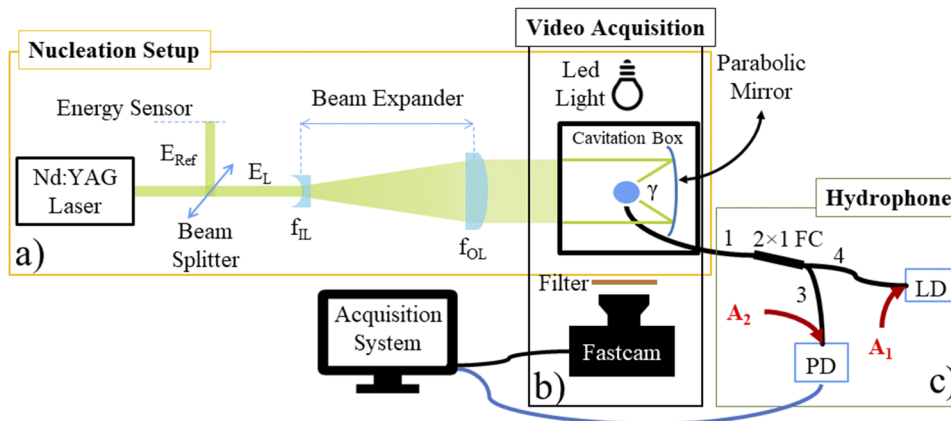
FIG. 1. Experimental setup. The system is divided into three main parts. (a) Bubble generation, based on a 532 nm Nd:YAG pulsed laser. The beam is expanded by a telescopic system and focused by an aluminum-coated parabolic mirror in a cavitation box. (b) High-speed video acquisition system. (c) Custom FOPH for pressure measurement of the shockwaves.

Before being focused, the laser beam is shaped by custom-made telescope systems to obtain different magnification values (×2, ×3, ×6, and ×8). The telescope is composed of two lenses with different focal lengths f: an imaging lens (f_{IL}) and an objective lens (f_{OL}). The ×3, ×6, and ×8 expansions are obtained by using a Galilean scheme, in which the image lens is a planoconcave spherical lens (f_{IL} = −25 mm) and the objective lens is a planoconvex spherical lens (f_{OL} = 75 mm, 150 mm, and 200 mm for ×3, ×6, and ×8, respectively). The ×2 expansion is obtained by using a Keplerian scheme (f_{IL} = 75 mm and f_{OL} = 150 mm).

The expanded and collimated beam is then introduced in the stainless-steel cavitation box (120 × 120 × 120 mm^3) that is provided with four quartz windows for optical access and two plates for instruments accommodation. One of these plates is equipped with a parabolic aluminum-coated mirror (Edmund Optics, diameter 50.8 mm, effective focal length f_{mir} = 54.45 mm) for beam focusing. The mirror, with nominal reflectance of 98% at 532 nm, has an off-axis focus point with an off-set β = 30°, and it is used to generate the cavitation bubble off the path of the incident beam.

Taking into account the magnification factors ×2, ×3, ×6, and ×8, the value of f_{mir}, the spot size (~4 mm), and the angular divergence (~2 mrad) of the laser beam, the focusing angles γ are 12°, 17°, 33°, and 53°, respectively.

B. Bubble imaging

The imaging system used to visualize the bubbles is schematically represented in Fig. 1(b). It consists of a Photron FastCam mini UX100 fast camera fitted with a Nikon Micro-Nikkor 105 mm f/2.8G IF-ED objective. The objective mounts a long wavelength pass filter, which is used to suppress the green pulsed laser at 532 nm, to avoid saturation and damage of the camera sensor. The camera was used at the frame rate of 64 kfps and 160 kfps, i.e., an interframing time of 15.6 μs and 6.25 μs, respectively. The active area of the camera sensor is varied depending on the frame rate, namely, 1280 × 72 pixels at 64 kfps and 1280 × 24 pixels at 160 kfps. The background illumination is provided by a LED. The cavitation bubbles appear black in the images, providing a clearly defined shadow.[21]

C. Pressure measurements

The most common hydrophones used for cavitation detection are based on piezoelectric polymers such as Polyvinylidene-Di-Fluoride (PVDF) or mechanical membranes. They are widely used in clinical imaging of biological tissues where the frequencies of interest are on the order of few tens of megahertz.[20] Being resonant mechanical systems, they must be miniaturized to reach higher frequencies.[42] The cost for a larger bandwidth is the reduction of mechanical robustness and sensitivity. Alternatively, fiber optics hydrophones have a much broader bandwidth and are sufficiently small and robust. Here, a custom made fiber optic probe hydrophone (FOPH) is used to measure the pressure signals emitted during breakdown. Our FOPH shows a smaller sensitivity in comparison to PVdF hydrophones due to a lower signal-to-noise ratio[26] but provides a much larger bandwidth.

The FOPH working principle is sketched in Fig. 1(c). The beam emitted by a CW (continuous wave) laser diode (LD) (Thorlabs,

830 nm, 1 W) is coupled by means of a lens to the input fiber (port 4) of a fiber coupler (FC) [Thorlabs, 2 × 1 Graded-Index (GRIN) Multimode, Thorlabs GIF625 fiber] with a nominally 3 dB splitting ratio. 50% of the transmitted power is coupled to the output fiber (port 1). The tip of this latter fiber is immersed in the cavitation box and is used as a pressure probe. 50% of the beam reflected at the end facet of the output fiber is coupled back to port 3 and is collected by a silicon avalanche photodetector (PD) (Thorlabs, APD430A2) with high sensitivity in the 200–1000 nm wavelength range and 400 MHz output bandwidth. The photodetector is connected to an oscilloscope (2440 Tektronix Digital Oscilloscope) with a maximum sampling rate of 500 megasamples/s for a real-time bandwidth of 200 MHz. Data are acquired and analyzed by a custom LabView software.

Pressure variations in the water in contact with the FOPH facet cause a density change and consequently a local change of the water refractive index and of the reflectance of the fiber/water interface. The latter variation is detected as a change in the photodetector voltage output. Because of the low glass compressibility, in comparison to water, the fiber refractive index changes are generally negligible.[26] The photodetector signal can be expressed as

$$V = A_1 A_2 \phi \frac{P_0}{4}(R + R_0), \qquad (3)$$

where P_0 is the laser diode power, ϕ is the conversion factor of the photodetector, and R_0 takes the signal noise into account. A_1 and A_2 are the LD/port 4 and port 3/PD coupling efficiencies, respectively, as shown in Fig. 1. R is the reflectance at the interface between the fiber probe and the external medium as expressed by the normal incidence Fresnel coefficient. The sensitivity S_R to a reflectance change, defined as

$$S_R = \frac{\partial V}{\partial R} = A_1 A_2 \phi \frac{P_0}{4}, \qquad (4)$$

is evaluated experimentally using liquids with different known refractive indexes. The response ΔV to a variation of pressure can be related to the reflectance change through the pressure sensitivity, S_p, which can be evaluated by combining the isentropic Tait equation, the Gladstone-Dale empirical relation for the water density as a function of the refractive index and the expressions of the Fresnel coefficients.[2] The expression for S_p is

$$S_p = \frac{\partial V}{\partial p} = S_R \frac{\partial R}{\partial p} = S_R \frac{4\sqrt{R}}{\kappa} \frac{n_f}{(n_f + n_l)^2} \frac{n_l^0 - 1}{p_0 + p_1} \left(\frac{p + p_1}{p_0 + p_1}\right)^{(1-\kappa)/\kappa}, \qquad (5)$$

where n_f = 1.496 and n_l^0 = 1.328 are the fiber and water refractive indexes, respectively, at 20 °C and atmospheric pressure. p_0 = 0.1 MPa, p_1 = 295.5 MPa, and κ = 7.44 are Tait's constants at 20 °C.[36] The constant S_p/S_R ratio is −6.63 × 10^{-6} MPa^{-1} at atmospheric pressure. S_p was evaluated every time the fiber probe was cleaved.

III. RESULTS AND DISCUSSION
A. Bubble dynamics and plasma shape

It is well known that a plasma is created in the focusing cone of a laser beam proximal to the laser. The plasma length is also known

to strongly depend on the focusing angle and the laser energy.[40,46] Moreover, multiple pointlike plasmas frequently occur.[40] Their formation has been mainly associated with impurities in the liquid and with focusing lenses' spherical aberrations.

Following Ref. 22, the present setup is optimized to prevent spherical aberrations through the use of the parabolic mirror. Therefore, spherical aberrations can be excluded as possible causes of plasma distortions. A further possible cause of asymmetry is the interaction with boundaries. Under this respect, the use of a mirror with a large focal length allows for minimizing/excluding this effect. Suitably placing the mirror inside the cavitation box ensures that the closest boundary is the surface of the mirror itself, with a distance to the bubble corresponding to the focal length. The parameter controlling boundary induced bubble asphericity is the so-called stand-off distance, defined as $\chi = h/r_{max}$, where h is the distance from the closest boundary (the mirror focal length for the present case) and r_{max} is the bubble radius at maximum expansion. A nearly spherical collapse is commonly reported for $\chi < 5$. Recently, "weak jets" piercing the bubble were detected for stand-off distances up to $\chi \sim 14$ (see Ref. 39). Therefore, the value $\chi > 27$ used in the present experiment safely excludes the boundaries as possible cause of asymmetries.

Hence, it is expected that the plasma shape principally depends on the parameters of the experiment, namely, focusing angle and laser pulse energy that are well controlled or directly measured in the experiments. Nevertheless, the random effect of liquid impurities remains among the possible reasons for plasma fragmentation.

Before going deeper into the plasma characteristics, bubble dynamics is shown in Fig. 2. Panel (a) reports the temporal evolution of the bubble radius at different focusing angles for the available highest laser energy E_L. For the larger focusing angles, two rebounds are apparent after the first collapse. In panel (b), the values of the maximum bubble radius r_{max} are plotted as a function of the laser energy E_L. Here, r_{max} is evaluated as the average over 64 consecutive events acquired at fixed laser energy. The bars attached to the data provide the standard deviation. Once the estimate of the maximum radius is available, Eq. (2) can be used to

estimate the (maximum) bubble potential energy, E_B, shown in panel (c). The ratio between E_B and E_L represents the amount of laser energy converted into bubble mechanical energy, ultimately responsible for bubble dynamics after breakdown and shockwave emission at collapse.[44] Increasing the focusing angle, the conversion efficiency of the present setup spans between 9% and 15%. The bubble dynamics obtained with the present experimental setup is in agreement with that already observed in the literature, as also reported in Ref. 35.

The effect of beam energy and focusing angle on plasma shape is illustrated in Figs. 3 and 4. Figure 3(a) shows a typical sequence of images acquired at 64 kfps used to extract information on the bubble dynamics. Panels b and c show the plasma shape (white/yellow spots) at different γ for two pulse energy values (left and right columns correspond to lower and higher energy, respectively). The bubble at maximum expansion is subtracted from each image and appears as an orange disk. The green arrow indicates the beam direction of incidence. Tightening the light cone, the plasma becomes thinner and elongated toward the laser source.

Figure 4 concerns the image gray scale I used to quantify the plasma light intensity. Panels (a) and (b) show the contour plots of $I(x, y)$, where x and y are the two coordinates in the image plane, for two focusing angles and different pulse energies. The intensity is normalized on the 8-bit depth of the images. Each image is obtained as the average over 64 bubble events captured at fixed (nominal) energy. The averaging procedure removes the random effects of the process, leaving only the deterministic influence of pulse energy and focusing angle on the plasma shape. The intensity profiles taken along the plasma main axis and spatially averaged over a 10-pixel wide strip, see panel (c), are shown in panels (d) and (e), corresponding to panels (a) and (b), respectively. As expected, by increasing the pulse energy E_L, the plasma tip keeps the same position while the tail shifts toward the light source (see also Fig. 3). At the same time, the peak intensity increases and the distribution broadens. At constant pulse energy, the focusing angle is found to crucially affect the energy distribution, which is more localized for wider angles.
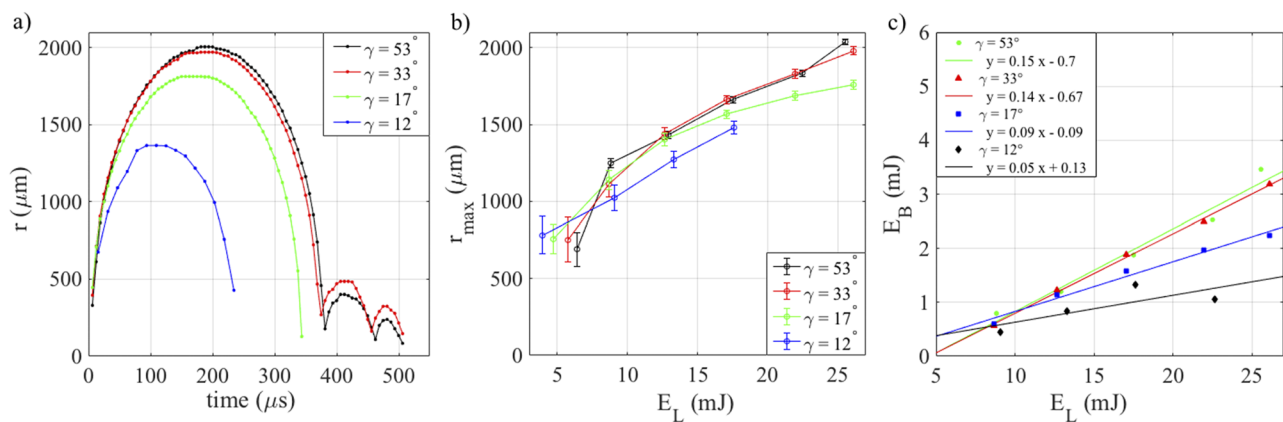
FIG. 2. Effect of the laser light focusing angle γ on the bubble dynamics. (a) Bubble radius evolution, (b) maximum bubble radius r_{max} as a function of the laser energy E_L, and (c) bubble potential energy E_B.
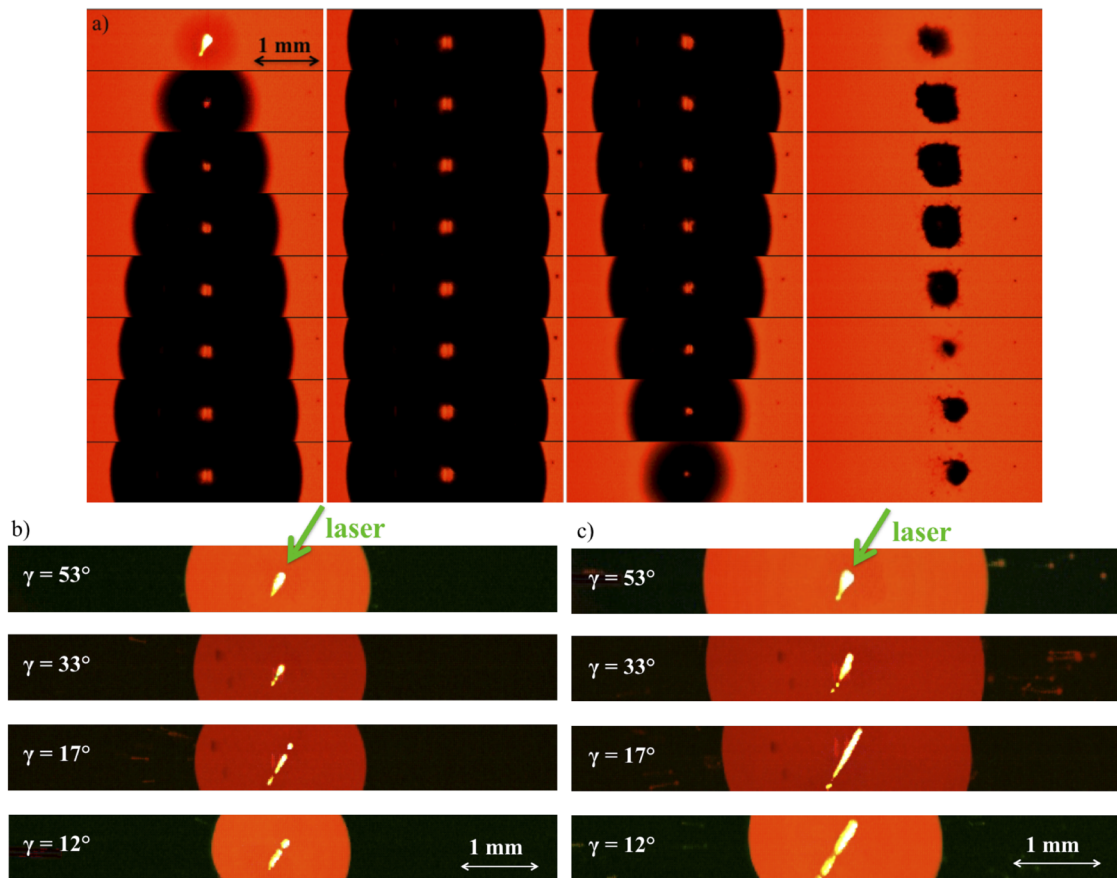
FIG. 3. (a) Images acquisition at 64 kfps corresponding to E_L = 22.0 mJ and γ = 53°. [(b) and (c)] Effect of the laser light focusing angle γ on the plasma shape. Composite images of the plasma (in yellow/white) and bubble at maximum expansion (orange disk) for E_L = 12.7 mJ (b) and E_L = 22.0 mJ (c). The direction of the laser beam is marked by the green arrows.

The plasma length L is plotted as a function of the energy E_L for different focusing angles in Fig. 5(a). It is measured between the two extremal points where the local intensity is one tenth of the maximum, more precisely the threshold values are I_{bg} + ((I_{max} − I_{bg})/10), with I_{bg} being the background. Well above the breakdown threshold energy E_{TH}, at the widest focusing angles (black and red symbols), L is almost unchanged with varying energy. For narrower light cones, L significantly depends on the angle γ and increases almost linearly with E_L (green and blue symbols). At the breakdown threshold, L is considerably shorter and becomes comparable to the maximum plasma thickness w, as illustrated through the sphericity index $\zeta(E_L, \gamma) = w/L$ plotted in Fig. 5(b) as a function of E_L which, at threshold, becomes ζ = 0.7–0.8. At large energy, the achievable sphericity is limited to $\zeta \leq 0.4$, regardless of the focusing angle.

Given the good sphericity achieved at the breakdown threshold energy, a few more details are provided for this case in Fig. 6. As already commented in Sec. I, the plasma shape can hardly be considered a purely deterministic process. Indeed, a substantial level of randomness is observed when repeating the experiments under the same nominal conditions. Statistics on plasma shapes at the breakdown threshold are shown in panel (a) of Fig. 6. The data refer to 64 consecutive acquisitions for each γ. The number of samples was found sufficient to assure reproducibility of the histogram. For example, for the case at focusing angle $\gamma = 12°$, doubling the data set changes the height of the histogram by less than 5%. As seen from the bars, the most frequent occurrence for any focusing angle is a single point plasma (see the examples of plasma shape reported below the panel). Panel (b) shows the increase in the threshold energy E_{TH} with γ. For given nominal conditions, the actual location of the plasma spot inside the light cone may fluctuate among the different realizations. Decreasing the focusing angle, the range of positions where the plasma may form increases as reported in panel (c), e.g., at $\gamma = 12°$, the plasma spot may appear within a ~600 μm long region. This random shift in the plasma location leads to a corresponding randomness in the bubble position. Histograms of the sphericity for the different plasma configurations are provided in panel (d) of Fig. 6.

Typically, after the first collapse, the bubble hardly achieves a spherical shape and may split into two or three daughter bubbles.
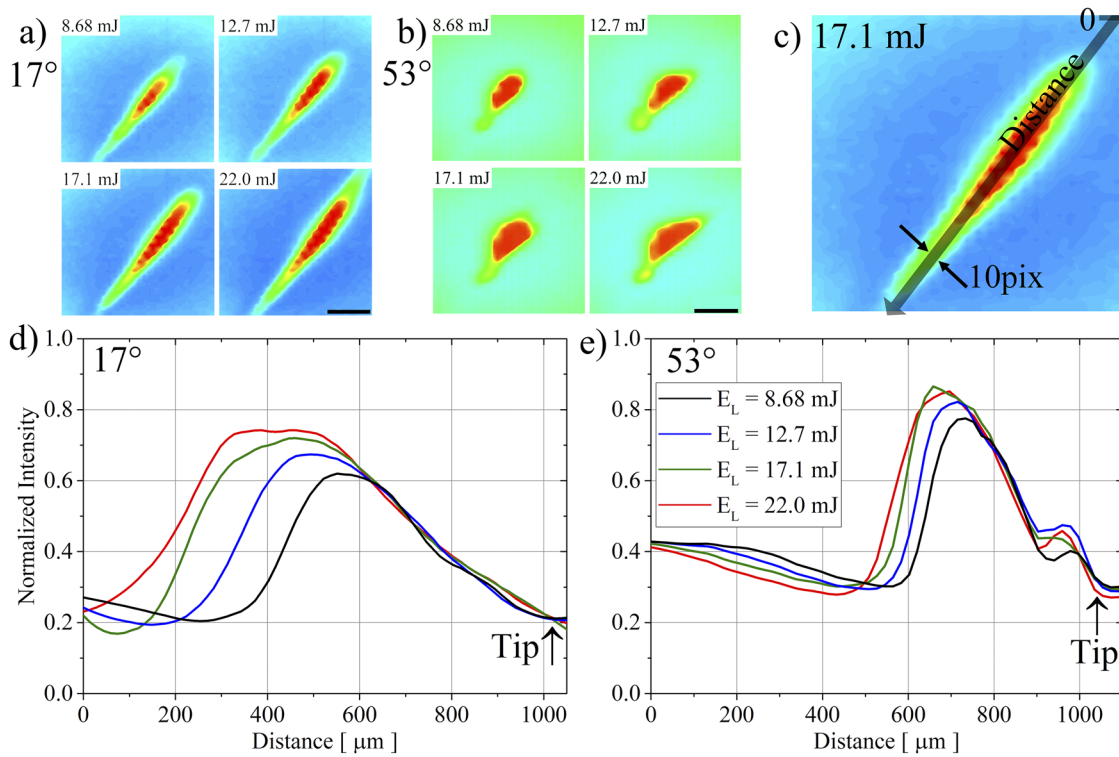
FIG. 4. Color map of the normalized gray scale intensity of the averaged plasma shape over 64 recordings for different energies and two focusing angles, 17° (a) and 53° (b). The plot (c) reports the process to measure the plasma length. The 2D graphs (d) and (e) are the intensity profiles along the plasma axis measured according to (c) for the cases shown in (a) and (b), respectively.

For the present setup, two conditions can be identified that lead to rebounds with a single bubble and high repeatability. The first condition corresponds to the breakdown threshold energy for all the focusing angles. The second one works at high laser energy and wide focusing angle. They are illustrated in Figs. 7(a) and 7(b), respectively. These figures are constructed by overlapping three frames corresponding to plasma appearance, bubble maximum expansion after inception and maximum expansion during the first rebound, respectively. In the composite image, the bubble configuration at rebound is shown as an orange disk inside the shadow shape of the bubble at maximum radius. Panel (a) reports two examples at threshold energy and $\gamma = 12°$. The plasma is point-like and the system is almost perfectly spherical and repeatable, except for the bubble center location which shows a certain level of randomness, as already discussed [see Fig. 6(c)]. Panel (b) reports a bubble obtained at $\gamma = 53°$ and $E_L = 26$ mJ. In this case, the plasma is conical with deterministic position. After the first collapse, an almost spherical single bubble usually rebounds, which is typically slightly displaced with respect to the center of the main bubble.
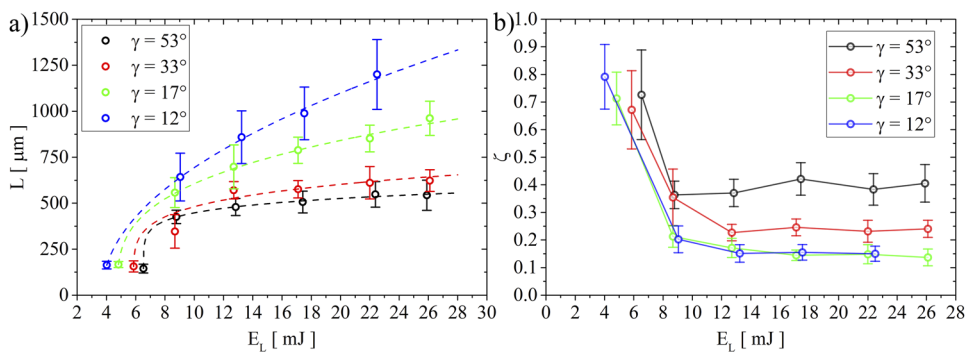
FIG. 5. Plasma length L (a) and plasma sphericity ζ (b) as a function of E_L.
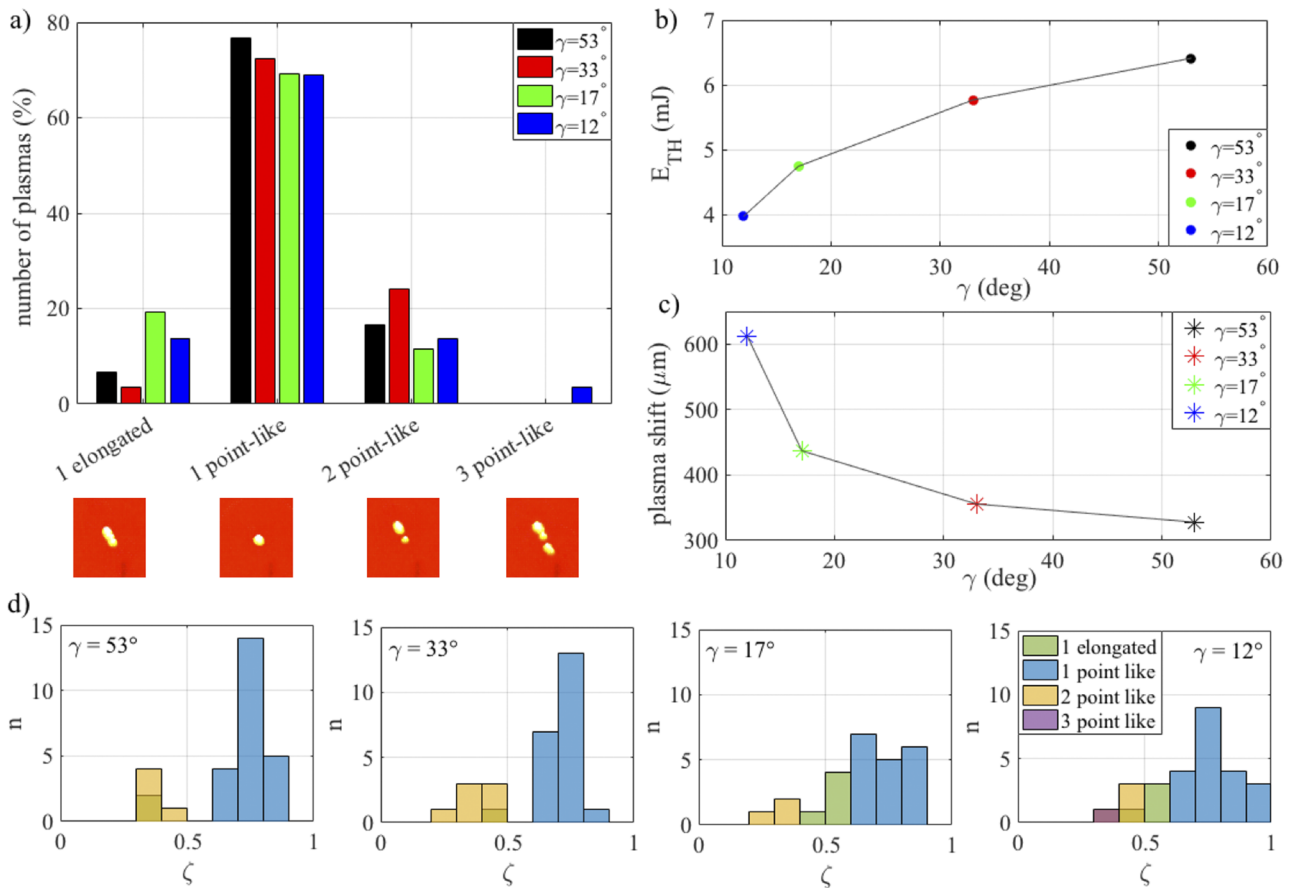
FIG. 6. Plasma formation at the breakdown threshold energy E_{TH}. (a) Histogram showing the occurrence of the different plasma configurations, (b) change of E_{TH} with γ, (c) shift of the plasma location with γ, and (d) histograms of the plasma sphericity ζ for the different plasma configurations.

B. Breakdown shockwave

Geometrically, the prevalent plasma feature is its conical elongated and, often, fragmented shape which significantly affects the shockwave system emitted at breakdown. The shockwave can be detected by using the hydrophone described in Sec. II C. Data are acquired at different positions, moving the sensor along the line parallel to the beam axis at the nominal distance d = 3 mm, as sketched

in panel (a) of Fig. 8. The data are obtained as a multipeak fit of the average obtained from 256 bubble cavitation events. To remove the effect of laser energy fluctuations, the signal acquisition was conditioned to the laser energy. Depending on the specific experiment, the accepted energy interval was chosen in the range of 1%–5% of the nominal pulse energy. Clearly, the signal read by the photodetector is contaminated by the laser pulse and plasma emission light peaks entering the probe. These contributions can be removed by
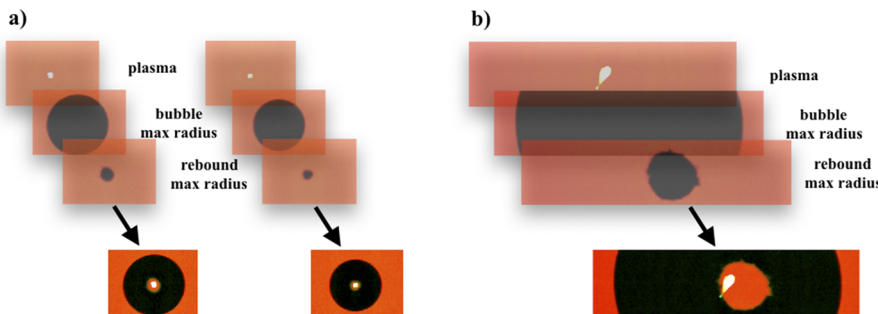
FIG. 7. Superimposition of three frames: plasma, bubble at maximum expansion after breakdown, and after the first rebound. (a) Examples of spherical-like plasma-bubble-rebound at the breakdown threshold energy $E_{TH} \approx 4$ mJ [see Fig. 6(b)] for γ = 12°, $R_{max} \sim 600$ μm (left) and $R_{max} \sim 500$ μm (right). (b) E_L = 26 mJ, γ = 53°, and R_{max} = 1970 μm.
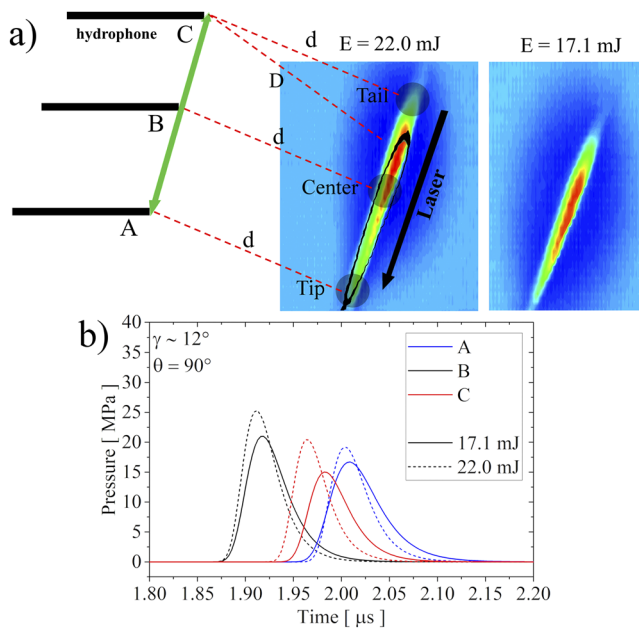
FIG. 8. (a) Position of the fiber probe for the study of the effect of the plasma shape on the pressure signal. The fiber was shifted along the direction parallel to the laser focusing direction at a nominal distance d = 3 mm (green arrow). D is the effective distance when the plasma shape changes. The two intensity graphs show how the shape changes when the laser energy is tuned. (b) Plot of the time dependent pressure signals for the three different positions shown in (a). The largest change of the peak maximum is observed at the plasma tail.

subtracting a reference signal acquired with the hydrophone laser diode switched off.

Figure 8 concerns the configuration with beam focusing angle $\gamma = 12°$. In panel (b), the pressure signal is plotted for two values of

the pulse energy, 17.1 and 22.0 mJ, and three positions of the sensor. With reference to the sketch in panel (a), point A is located in correspondence to the leading edge of the 22.0 mJ-pulse plasma, point B is in the middle and point C corresponds to the trailing edge. As discussed in Sec. III A, the 17.1 mJ-pulse plasma is shorter, see the corresponding black contour superimposed to the higher energy plasma in panel (a). Being determined by the optical arrangement, the leading edge is the same in both cases, implying that, in position C, the sensor is in fact farther from the plasma trailing edge for the lower pulse energy.

The shockwave is strongly sensitive to the plasma shape and intensity, with pressure peak amplitude and arrival time depending on sensor position and laser pulse energy. Increasing the laser energy, the pressure wave amplitude increases and the arrival time reduces. Typically, a difference of about 4–5 ns is observed for the two energies when the sensor is positioned in correspondence with the plasma leading edge (A) and the plasma center (B). This is consistent with the increased shockwave intensity which entails a faster propagation speed. In addition, when moving the sensor to C, the delay time between the two energies is also affected by the different distance between sensor and plasma trailing edge. As a consequence, the delay increases by about ~18 ns consistently with the estimate based on distance [difference $D - d \sim 15~\mu$m in panel (a)] and typical sound speed.

From panel (b) of Fig. 8, the pressure peak is larger in point B (middle) with respect to those in A and C (tips). This reasonably suggests that the wave is formed by the superposition of signals originating from different spots in the plasma region.

In order to enhance this effect and understand the structure of the wave, the hydrophone position is moved along a circle coplanar with the laser beam axis and centered on the bubble (see also Ref. 40). Given the distance d from the plasma, the hydrophone position is identified by the angle θ in Fig. 9(a). The pressure signals collected at $\theta = 0°$, $45°$, $90°$ for different focusing angles of the laser
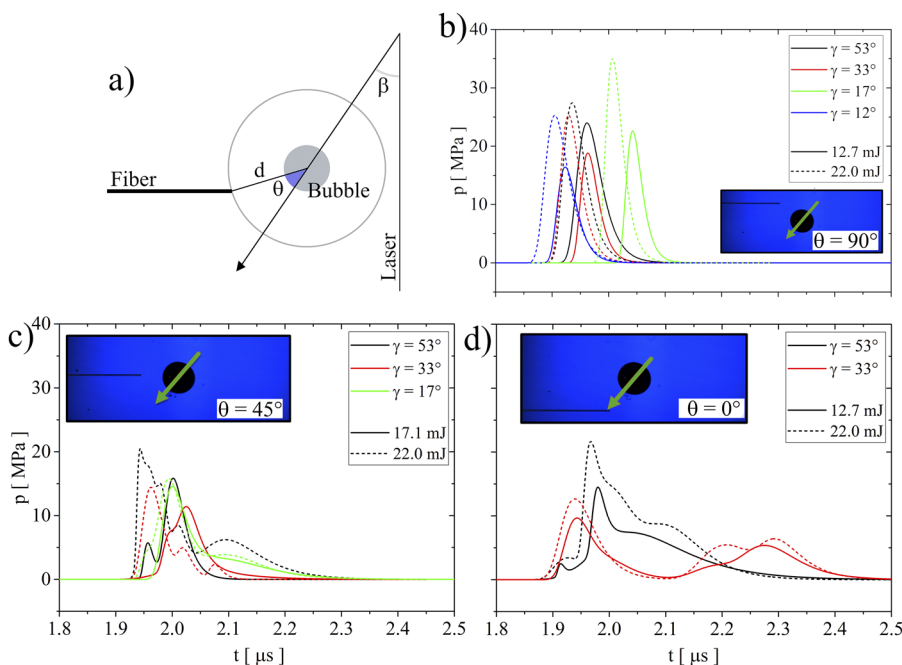
FIG. 9. (a) Relative position of the fiber tip with respect to the focusing point of the pulsed laser (the sketch is rotated 90° counterclockwise with respect to the actual configuration with the vertical hydrophone axis). Pressure measurements of breakdown shockwave: (b) $\theta = 90°$, (c) $\theta = 45°$, and (d) $\theta = 0°$. The insets show the image of the bubble and the hydrophone. The green arrow indicates the laser beam propagation path and direction.

beam and two pulse energies are shown in Figs. 9(b)–9(d). Like for the hydrophone configuration B in Fig. 8, a single peak is observed at $\theta = 90°$ with a delay with respect to the laser pulse trigger that depends on γ and E_L [see Fig. 9(b)]. The peak increases in intensity and shifts monotonically to earlier times when the laser energy is increased (see the dashed lines), for all focusing angles, a result that is in agreement with the observed shockwave velocity increase associated with larger shock strengths.[40,45] Changing the angular position, the wave tends to split in distinct components. Multiple peaks clearly appear at $\theta = 45°$ and $0°$, see Figs. 9(c) and 9(d), confirming recent results, respectively.[40] Moving from $90°$ (FOPH orthogonal to the beam axis) to $0°$ (FOPH along the direction of the beam), the peaks spread apart increasingly more along the time axis. This effect is more pronounced for narrower focusing angles, consistently with the more pronounced axial elongation of the plasma shown in Sec. III A.

The pressure level discussed so far is the absolute pressure measured by the hydrophone. In order to determine the actual amplitude of the incoming pressure wave, the pressure signal must be corrected to take into account the acoustic reflections at the water/hydrophone fiber tip interface. Indeed, the pressure is the sum of the incident pressure wave to be measured and the pressure due to wave reflected at the fiber tip. To account for this effect, the data taken from the FOPH are corrected reducing the measured values by a factor C that is estimated by assuming a planar incident wave reflected by the planar facet of the sensor (fiber core diameter of 62.5 μm, with overall—core plus cladding—transversal size of 125 μm). To evaluate C, the relevant parameters are the sound speed in water ($c = 1450$ m/s) and in the fiber ($c_{fiber} = 5760$ m/s)[3] and the incidence angle α of the pressure wave with respect to the normal to the facet. As shown in Fig. 9, $\alpha = 90° - \theta - \beta$, where θ identifies the position of the hydrophone tip and β the direction of the laser beam. We assumed that the fiber tip cleavage plane is normal to the fiber axis. In the experimental setup, the fiber was hanging vertically downward and the nucleation beam was inclined upward by the off-set angle of the parabolic mirror $\beta = 30°$ with respect to the horizontal plane. For the three positions of the fiber tip, $\theta = 0°, 45°, 90°$, we had $\alpha = 60°, 15°, -30°$, respectively. When reaching the fiber tip, the acoustic wave could be partially reflected back in water and partially transmitted inside the fiber. However, since $c_{fiber} > c$, a critical incidence angle exists $\delta = \sin^{-1}(n)$ with $n = c/c_{fiber}$,[3] above which the pressure wave is totally reflected in water. In all cases reported here, $|\alpha| > \delta = 14.58°$ and the pressure wave was always totally reflected. Under such conditions, the (acoustic) pressure reflection coefficient is complex $R_{ac} = e^{J\phi}$[3] with phase angle $\phi = -2\arctan\left(\sqrt{\sin^2\alpha - n^2}/m\cos\alpha\right)$, where $m = \rho_{fiber}/\rho = 2.4$ is the fiber-to-water mass density ratio.[10] The resulting pressure field at the fiber facet is then $p = Re[A(1 + e^{J\phi})e^{-J\omega t}]$, where Re denotes the real part of the complex number and A is the amplitude of the incident pressure wave. With some simple analytical steps, we get $p = Re[A\sqrt{2(1 + \cos\phi)}e^{-J(\omega t + \psi)}]$, where $A\sqrt{2(1 + \cos\phi)}$ is the amplitude of the resulting pressure and $\tan(\psi) = \sin(\phi)/(1 + \cos(\phi))$. Consequently, the pressure normalization factor is $C = \sqrt{2(1 + \cos\phi)}$, which corresponds to $C = 1.64, 1.99, 1.96$ for the three tip positions θ, respectively.

The peak pressure values measured during the experiments and reduced by the factor C are reported in Fig. 10 for the two largest
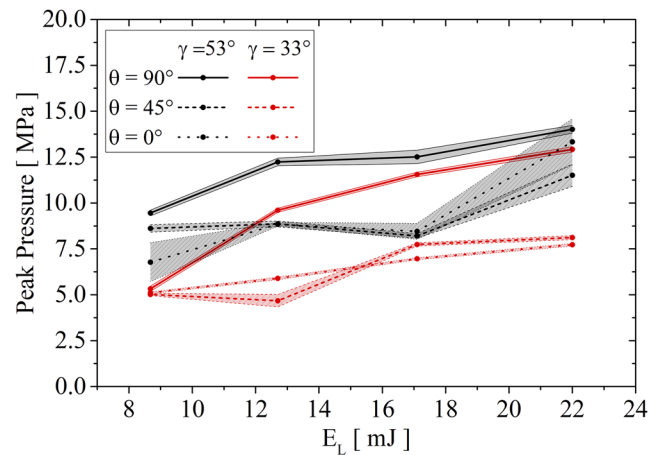
FIG. 10. Peak pressure of the laser-induced underwater shockwave.

focusing angles γ. The maximum peak pressure values are found for $\theta = 90°$ (continuous lines), where it increases monotonically with respect to the laser pulse energy. In general, the peak pressure at $\theta = 45°$ (dashed) is higher than at $\theta = 0°$ (dotted). However, the peak pressure changes irregularly with the laser pulse energy, presumably due to different fragmentation modes of the plasma structure.

From the hydrophone data, a reconstruction of the breakdown shockwave system can be attempted by assuming a superposition of different spherical wavefronts, each originating from different locations of the plasma, as shown in Fig. 9, see also Refs. 34 and 40. Such reconstruction is sketched in Fig. 11 for $\gamma = 33°$, $E_L = 26.1$ mJ (top) and $\gamma = 53°$, $E_L = 17.1$ mJ (bottom). Given the elongated plasma shape, the shockwave system is spread along the direction of the laser beam. In both cases, the hydrophone detects three distinct pressure peaks, suggesting that, on average, the plasma generates three waves from three different locations. The strength of each wave is strongly sensitive to the specific experimental conditions, e.g., laser beam energy and focusing angle. In particular, Figs. 11(a) and 11(c) show that the highest pressure at the fiber location $\theta = 0°$ is, respectively, associated with the first and second wavefronts reaching the fiber tip. At $\theta = 45°$, the peaks get temporally closer, see red curves in the same figures, and eventually merge in a single wave pulse at $\theta = 90°$ (black curves) implying that the three wave components almost simultaneously reach the FOPH in this location.

The pressure signals can also be used to qualitatively infer information on the initial stages of the bubble (a timeframe of about ~500 ns) suggesting that it is formed by the coalescence of three distinct vapor embryos, consistently with the plasma structures that give rise to the detected pressure waves [Figs. 11(b) and 11(d)]. One may conjecture that the highest intensity shockwave is associated with the largest initial bubble embryo that, by expanding, coalesces with the neighbors to produce the single cavitation bubble that is successively imaged by the camera. The above comments highlight the initial asymmetry of the bubble which, during the expansion, becomes more and more spherically symmetric. However, perfect spherical symmetry is hardly achieved.
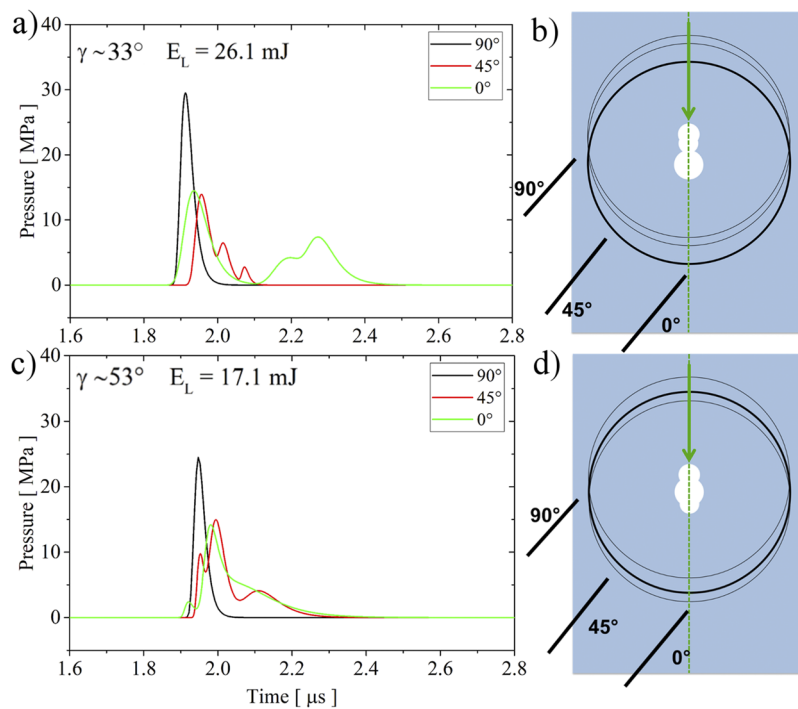
FIG. 11. Reconstruction of the breakdown shockwaves and the first instants of the bubble lifetime (~500 ns) from the pressure signals. $\gamma = 33°$ [(a) and (b)] and $\gamma = 53°$ [(c) and (d)]. The shockwaves associated with the largest bubble embryo are highlighted in (b) and (d).

The residual asymmetry is amplified during the successive collapse phase,[15,37] leading to the asymmetric rebound that is most often observed.

IV. CONCLUSIONS

Laser induced cavitation, where a cavitation bubble is formed as a consequence of a pulsed laser beam focused in water, has been addressed. As well known, after energy deposition, the bubble expands to a maximum radius and then collapses leading to a sequence of rebounds. The subject is of strong interest on its own and as a controlled way to produce cavitation bubbles for basic study and for exploitation in many different applications, in technology and medicine. Plasma formation due to the intense electric field is confirmed to be a stochastic process depending on several parameters, among which laser beam focusing angle, laser pulse energy and duration, laser stability, optical aberrations, and water impurities. Most of these parameters can be controlled, at least partially, by using pure water, by employing a parabolic mirror to prevent spherical aberrations in the focusing optics, or by conditioning the data acquisition to the actual pulse energy of each single realization.

The purpose of the present work was to focus on the repeatability of the laser induced cavitation process, and specifically on the effect of the beam focusing angle and pulse energy (once minimized the effect of the other parameters), as these two factors strongly affect the shape and strength of the triggering plasma.

In this paper, different plasma configurations have been analyzed using fast camera visualizations. The data allowed us to determine the shape of the breakdown region and capture the plasma intensity distribution as a function of energy deposition and beam focusing angle. The plasma takes an elongated and often fragmented, conical shape with a trailing edge determined by the focusing optics and with the plasma region extending in the light cone proximal to the light source.

Bubble dynamics following breakdown is correlated with the plasma shape. Within the present accuracy limitation, the first bubble forming after breakdown reaches always a spherical symmetry. On the contrary, the rebound bubble suffers significant asymmetries, often fragmenting into multiple daughter bubbles. The probability of obtaining a spherical rebound is found to depend on the plasma structure. Two conditions have been identified to optimize sphericity. One is enabled by a large focusing angle combined with a relatively large pulse energy, a process which retains a stochastic nature, leading to conical shaped plasmas with a repeatable location. The other corresponds to the almost opposite condition where the pulse energy is kept at the threshold for breakdown, independently of the focusing angle. In this case, the plasma is pointlike with random position within a certain region of the light cone, consistently with local electric field fluctuations presumably related to local impurities. In this condition, a spherically symmetric rebound dynamics is achieved almost deterministically.

Plasma shape and fragmentation define the structure of the bubble embryos, as reconstructed by the analysis of the shockwave system initiated at breakdown. In order to detect and measure the intensity of the shockwaves, a custom-made fiber optic probe hydrophone was assembled. The pressure signal has been measured at different positions to reconstruct the wave structure. Plasma shape, elongated and/or fragmented in most cases, is found to

correlate with nonspherically symmetric shockwave emission at breakdown.

This work clarifies the effect of two central design parameters for laser induced cavitation, suggesting new guidelines to ensure the repeatability of the process thereof.

REFERENCES

[1] I. Akhatov, O. Lindau, A. Topolnikov, R. Mettin, N. Vakhitova, and W. Lauterborn, "Collapse and rebound of a laser-induced cavitation bubble," Phys. Fluids **13**, 2805–2819 (2001).

[2] A. Arvengas, K. Davitt, and F. Caupin, "Fiber optic probe hydrophone for the study of acoustic cavitation in water," Rev. Sci. Instrum. **82**, 034904 (2011).

[3] L. M. Brekhovskikh and O. A. Godin, *Acoustics of Layered Media I: Plane and Quasi-Plane Waves* (Springer Science & Business Media, 2012), Vol. 5.

[4] C. E. Brennen, *Cavitation and Bubble Dynamics* (Cambridge University Press, 2014).

[5] C. E. Brennen, "Cavitation in medicine," Interface Focus **5**, 20150022 (2015).

[6] E. Brujan, G. Keen, A. Vogel, and J. Blake, "The final stage of the collapse of a cavitation bubble close to a rigid boundary," Phys. Fluids **14**, 85–92 (2002).

[7] E.-A. Brujan and A. Vogel, "Stress wave emission and cavitation bubble dynamics by nanosecond optical breakdown in a tissue phantom," J. Fluid Mech. **558**, 281–308 (2006).

[8] F. Caupin and E. Herbert, "Cavitation in water: A review," C. R. Phys. **7**, 1000–1017 (2006).

[9] B. Han, L. Liu, and X.-W. Ni, "Investigation of the interaction dynamics of a pair of laser-induced bubbles generated at the same time through double-exposure strobe method and numerical simulations," Phys. Fluids **29**, 087103 (2017).

[10] W. M. Haynes, *CRC Handbook of Chemistry and Physics* (CRC Press, 2014).

[11] P. K. Kennedy, D. X. Hammer, and B. A. Rockwell, "Laser-induced breakdown in aqueous media," Prog. Quantum Electron. **21**, 155–248 (1997).

[12] W. Lauterborn, "High-speed photography of laser-induced breakdown in liquids," Appl. Phys. Lett. **21**, 27–29 (1972).

[13] W. Lauterborn and H. Bolle, "Experimental investigations of cavitation-bubble collapse in the neighbourhood of a solid boundary," J. Fluid Mech. **72**, 391–399 (1975).

[14] W. Lauterborn, T. Kurz, C. Schenke, O. Lindau, and B. Wolfrum, "Laser-induced bubbles in cavitation research," in *IUTAM Symposium on Free Surface Flows* (Springer, 2001), pp. 169–176.

[15] W. Lauterborn and A. Vogel, "Shock wave emission by laser generated bubbles," Shock Waves **8**, 67–103 (2013).

[16] Z. Li, K. Luo, C. Ohl, J. Zhang, and A. Liu, "A single-cell membrane dynamic from poration to restoration by bubble-induced jetting flow," in *Proceedings for the 15th International Conference on Miniaturized Systems for Chemistry and Life Sciences* (Chemical and Biological Microsystems Society, 2011), pp. 94–96.

[17] K. Y. Lim, P. A. Quinto-Su, E. Klaseboer, B. C. Khoo, V. Venugopalan, and C.-D. Ohl, "Nonspherical laser-induced cavitation bubbles," Phys. Rev. E **81**, 016308 (2010).

[18] F. Magaletti, M. Gallo, L. Marino, and C. M. Casciola, "Shock-induced collapse of a vapor nanobubble near solid boundaries," Int. J. Multiphase Flow **84**, 34–45 (2016).

[19] F. Magaletti, L. Marino, and C. M. Casciola, "Shock wave formation in the collapse of a vapor nanobubble," Phys. Rev. Lett. **114**, 064501 (2015).

[20] P. Morris, A. Hurrell, A. Shaw, E. Zhang, and P. Beard, "A Fabry–Pérot fiber-optic ultrasonic hydrophone for the simultaneous measurement of temperature and acoustic pressure," J. Acoust. Soc. Am. **125**, 3611–3622 (2009).

[21] D. Obreschkow, M. Tinguely, N. Dorsaz, P. Kobel, A. De Bosset, and M. Farhat, "Universal scaling law for jets of collapsing bubbles," Phys. Rev. Lett. **107**, 204501 (2011).

[22] D. Obreschkow, M. Tinguely, N. Dorsaz, P. Kobel, A. De Bosset, and M. Farhat, "The quest for the most spherical bubble: Experimental setup and data overview," Exp. Fluids **54**, 1502 (2013).

[23] A. Occhicone, G. Sinibaldi, N. Danz, C. M. Casciola, and F. Michelotti, "Cavitation bubble wall pressure measurement by an electromagnetic surface wave enhanced pump-probe configuration," Appl. Phys. Lett. **114**, 134101 (2019).

[24] C.-D. Ohl, M. Arora, R. Dijkink, V. Janve, and D. Lohse, "Surface cleaning from laser-induced cavitation bubbles," Appl. Phys. Lett. **89**, 074102 (2006).

[25] C.-D. Ohl, T. Kurz, R. Geisler, O. Lindau, and W. Lauterborn, "Bubble dynamics, shock waves and sonoluminescence," Philos. Trans. R. Soc., A **357**, 269–294 (1999).

[26] J. E. Parsons, C. A. Cain, and J. B. Fowlkes, "Cost-effective assembly of a basic fiber-optic hydrophone for measurement of high-amplitude therapeutic ultrasound fields," J. Acoust. Soc. Am. **119**, 1432–1440 (2006).

[27] F. Pereira, F. Avellan, and P. Dupont, "Prediction of cavitation erosion: An energy approach," J. Fluids Eng. **120**, 719–727 (1998).

[28] G. Peruzzi, G. Sinibaldi, G. Silvani, G. Ruocco, and C. M. Casciola, "Perspectives on cavitation enhanced endothelial layer permeability," Colloids Surf., B **168**, 83–93 (2018).

[29] A. Philipp and W. Lauterborn, "Cavitation erosion by single laser-produced bubbles," J. Fluid Mech. **361**, 75–116 (1998).

[30] M. S. Plesset, "The dynamics of cavitation bubbles," J. Appl. Mech. **16**, 277–282 (1949).

[31] Lord Rayleigh, "On the pressure developed in a liquid during the collapse of a spherical cavity," London, Edinburgh, Dublin Philos. Mag. J. Sci. **34**, 94–98 (1917).

[32] C. Sacchi, "Laser-induced electric breakdown in water," J. Opt. Soc. Am. B **8**, 337–345 (1991).

[33] G. Sankin, F. Yuan, and P. Zhong, "Pulsating tandem microbubble for localized and directional single-cell membrane poration," Phys. Rev. Lett. **105**, 078101 (2010).

[34] G. N. Sankin, Y. Zhou, and P. Zhong, "Focusing of shock waves induced by optical breakdown in water," J. Acoust. Soc. Am. **123**, 4071–4081 (2008).

[35] G. Sinibaldi, A. Occhicone, F. Alves Pereira, D. Caprini, L. Marino, F. Michelotti, and C. M. Casciola, "Laser induced breakdown and bubble cavitation," in *Proceedings of the 10th International Symposium on Cavitation (CAV2018)* (ASME Press, 2018).

[36] J. Staudenraus and W. Eisenmenger, "Fibre-optic probe hydrophone for ultrasonic and shock-wave measurements in water," Ultrasonics **31**, 267–273 (1993).

[37] H. Strube, "Numerical investigations on the stability of bubbles oscillating nonspherically," Acta Acust. Acust. **25**, 289–303 (1971).

[38] O. Supponen, P. Kobel, D. Obreschkow, and M. Farhat, "The inner world of a collapsing bubble," Phys. Fluids **27**, 091113 (2015).

[39] O. Supponen, D. Obreschkow, M. Tinguely, P. Kobel, N. Dorsaz, and M. Farhat, "Scaling laws for jets of single cavitation bubbles," J. Fluid Mech. **802**, 263–293 (2016).

[40] Y. Tagawa, S. Yamamoto, K. Hayasaka, and M. Kameda, "On pressure impulse of a laser-induced underwater shock wave," J. Fluid Mech. **808**, 5–18 (2016).

[41] Y. Tomita and A. Shima, "High-speed photographic observations of laser-induced cavitation bubbles in water," Acta Acust. Acust. **71**, 161–171 (1990).

[42] E. Vannacci, L. Belsito, F. Mancarella, M. Ferri, G. Veronese, A. Roncaglia, and E. Biagi, "Miniaturized fiber-optic ultrasound probes for endoscopic tissue analysis by micro-opto-mechanical technology," Biomed. Microdevices **16**, 415–426 (2014).

[43] V. Venugopalan, A. Guerra III, K. Nahen, and A. Vogel, "Role of laser-induced plasma formation in pulsed cellular microsurgery and micromanipulation," Phys. Rev. Lett. **88**, 078103 (2002).

[44] A. Vogel, S. Busch, K. Jungnickel, and R. Birngruber, "Mechanisms of intraocular photodisruption with picosecond and nanosecond laser pulses," Lasers Surg. Med. **15**, 32–43 (1994).

[45] A. Vogel, S. Busch, and U. Parlitz, "Shock wave emission and cavitation bubble generation by picosecond and nanosecond optical breakdown in water," J. Acoust. Soc. Am. **100**, 148–165 (1996).

[46] A. Vogel, K. Nahen, D. Theisen, and J. Noack, "Plasma formation in water by picosecond and nanosecond Nd:YAG laser pulses. I. Optical breakdown at threshold and superthreshold irradiance," IEEE J. Sel. Top. Quantum Electron. **2**, 847–860 (1996).

[47] A. Vogel, J. Noack, G. Hüttman, and G. Paltauf, "Mechanisms of femtosecond laser nanosurgery of cells and tissues," Appl. Phys. B **81**, 1015–1047 (2005).

[48] A. Vogel, J. Noack, K. Nahen, D. Theisen, S. Busch, U. Parlitz, D. Hammer, G. Noojin, B. Rockwell, and R. Birngruber, "Energy balance of optical breakdown in water at nanosecond to femtosecond time scales," Appl. Phys. B **68**, 271–280 (1999).

[49] B. Wolfrum, T. Kurz, R. Mettin, and W. Lauterborn, "Shock wave induced interaction of microbubbles and boundaries," Phys. Fluids **15**, 2916–2922 (2003).

[50] S. Zhu, F. H. Cocks, G. M. Preminger, and P. Zhong, "The role of stress waves and cavitation in stone comminution in shock wave lithotripsy," Ultrasound Med. Biol. **28**, 661–671 (2002).

[51] E. Zwaan, S. Le Gac, K. Tsuji, and C.-D. Ohl, "Controlled cavitation in microfluidic systems," Phys. Rev. Lett. **98**, 254501 (2007).

[52] B. Zysset, J. Fujimoto, and T. Deutsch, "Time-resolved measurements of picosecond optical breakdown," Appl. Phys. B **48**, 139–147 (1989).